

Final Report on NASA Grant NAG-1-1816
**EXPERIMENTAL STUDY OF COMPLEX VORTEX
INTERACTIONS IN THE WAKE OF HIGH
ASPECT RATIO WINGS**

Principal Investigator: Professor Ömer Savas
Department of Mechanical Engineering
University of California, Berkeley, CA 94720-1740
(510) 642-5705 (tel), (510) 642-6163 (fax), savas@euler.me.berkeley.edu

August 6, 1997

Abstract

The dynamics of trailing vortex wakes from flapped airfoils are investigated in a towing tank and a wind tunnel. In this work, parallel experiments are conducted in a wind tunnel with a five-hole probe for near wake measurements and in a tow tank with particle image velocimetry (PIV) for mid- and far-wake measurements. The wind tunnel allows detailed time-averaged measurements of the near-wake in a plane fixed relative to the wing while the tow tank allows measurements of the entire evolving wake in a plane fixed relative to an observer.

The wakes from a lifting rectangular circular arc airfoil with an aspect ratio of 6 and flap-spans of 30% and 67% and a NACA 0012 with an aspect ratio of 8 and flap-spans of 40% and 50% are studied as the wake evolves downstream. Chord-based Reynolds number Re_c ranged from $1.5 \cdot 10^4$ to $8 \cdot 10^4$. A traversing five-hole pitot probe and Lagrangian Parcel Tracking (LPT) are used to measure the velocity field in a cross-stream plane behind the wing in the wind tunnel and the towing tank, respectively. The interaction of the tip and flap vortices are studied. Merger of the flap and tip vortices usually occurs within one orbit, leading to a shorter descent distance to merger for the longer flap-spans. The strut wake significantly effects the vortex strength, hence merger characteristics, by disrupting the vortex sheet.

Contents

1	Introduction	2
1.1	Previous Work	2
1.2	Current Work	2
2	Experimental Apparatus	3
2.1	Airfoil Selection	3
2.2	Wind Tunnel Setup	4
2.3	Towing Tank Setup	4
2.4	Data Processing	5
2.4.1	5-hole Pitot Probe	5
2.4.2	Lagrangian Parcel Tracking	5
3	Data Analysis	6
3.1	Wind Tunnel	6
3.1.1	Probe Effect	6
3.1.2	Wake Decomposition	7
3.2	Tow Tank	8
3.2.1	Effects of Stratification	8
3.2.2	Flow Visualization	8
3.2.3	LPT Results	9
4	Results	9
4.1	The Strut Wake	9
4.2	Angle of Attack and Wing Stall	10
4.3	Vortex Merger	10
5	Summary	13
A	Tables & Figures	16
B	Wind Tunnel Vorticity Plots	26

1 Introduction

1.1 Previous Work

The trailing vortex wake is a physical phenomenon that has maintained a persistent level of interest in many communities, from both a scientific and an engineering standpoint. The importance of this problem has grown in recent years, due in part to FAA/NASA interest in the cause of some aircraft accidents, which have been partially attributed to the action of the vortex pair located in the vortex wake on the aircraft in question [1, 2]. The problem is also logistical (thus, economical as well) with FAA restrictions on aircraft separation resulting in limitations on airport capacity (e.g, see [3, 4, 5]). From a scientific standpoint, this renewed interest can be accredited to better methods of experimental and numerical investigation which have been developed in the last decade. On the experimental side, we are able to make field measurements with ease. Most notably, the use of Particle Image Velocimetry (PIV) techniques in the measurement of flow fields has grown substantially [6, 7, 8]. Previously, measurements of the wake vortex of a rectangular wing have been made using this technique [9, 10, 11]. From these measurements, modifications have been made to similar airfoils to study more complex physical phenomena. The goals are twofold:

1. to understand the fundamental physics of vortex interaction, such as that encountered among the wingtip and flap vortices in the wake of an aircraft and
2. to study how these interactions change when the initial conditions are made more complex (or “realistic”), such as by adding engines with and without thrust or fuselage wake effects.

In the case of multiple vortex wake interactions, there is debate on the merger process between the flap vortices and the wingtip vortices. The interest here lies in the dynamics. Particular interest has been placed upon when, or if, the vortices will merge for a given configuration. Some numerical analyses have predicted that the vortices may never merge under certain conditions (e.g., see [12, 13, 14]), though the chaotic nature of the multi-bodied problem suggests otherwise (e.g., see [15]).

1.2 Current Work

This work examines the vortex wake of a lift-generating flapped airfoil. The intent is to study the vortex interaction of the like-signed vortices within the wake. A lifting wing with a single flap develops a system of two vortex pairs; one each from the wing tips and flap tips. The vortices within each pair will be co-rotating while the pairs themselves will be counter-rotating. It is the dynamics of the co-rotating (same signed) vortices that interest us here. For a wing of sufficiently

high aspect ratio, the same signed vortices will behave independently of the opposite signed vortex pair, in effect behaving as an isolated co-rotating vortex pair under an induced downwash.

Two techniques are used to study the problem at hand: five-holed pitot probe measurements in a wind tunnel, and planar velocimetry measurements in a towing tank. The former technique has the benefit of analyzing the wake in a controlled manner since the position of the vortices are known a priori for a given downstream measurement location. Since the probe measures the steady (time-averaged) three-dimensional velocity field of the wake, gross quantities such as axial velocity, vortex strength, etc., are easily found. The latter method, while more complex, gives instantaneous time-dependent data required to study the merger process in detail. Measurements of this type are more difficult to obtain, but the additional information gained outweigh the increased complexity. It is hoped that the two techniques compliment one another, so that observations made in one can be confirmed in another. Also, each has advantages over the other, such as axial flow measurements in the case of the five-holed pitot probe and time dependent vortex motion in the planar velocimetry experiments.

2 Experimental Apparatus

2.1 Airfoil Selection

In the experiments, the airfoil is a rectangular plan-form with a circular arc profile constructed of 1.1mm thick stainless steel sheet. Two airfoils are available. Both airfoils have span $b = 305$ mm and chord $c = 51$ mm, giving an aspect ratio of 6. The radius of curvature of the camber is 128 mm. Step-changes in lift distribution are obtained with flap extensions of $c/3$ -wide beyond the trailing edge. Two flap-spans are available: 30% (short flap) and 67% (long flap). The airfoil is attached to the wind tunnel ceiling or to the towing carriage by a strut mounted to the airfoil centerline. The strut to the carriage is either a thick streamlined strut (approximated by a NACA 0030 profile with a chord length of 25 mm and a blunt trailing edge) or a thin flat plate strut (chord of 25 mm and 3.2 mm thick with faired leading and trailing edges). The angle of attack α of the airfoils is variable from -12° to $+12^\circ$ in 2° increments. The wing planform is shown in figure 1.

Four engine pods may be mounted on either wing in one or two pairs. The pods are constructed of stainless steel and are mounted to the wing using streamlined brass struts with a NACA 0012 profile at 30% and 70% span locations. The engine pods are 40mm long and 15 mm in diameter. The leading edge of the pods have a 2:1 elliptical profile and the trailing edge is faired to provide a smooth transition with the freestream. Steel tubing leads from a high pressure reservoir down the strut and beneath wings to the engines, though the runs herein consider the jets in a zero-thrust mode. The engines are shown in figure 3.

2.2 Wind Tunnel Setup

The wind tunnel experiments are conducted in the University of California-Berkeley low-turbulence low speed wind tunnel. The wind tunnel has a square test section measuring 0.81 m square and is 3.7 m long. The test section side walls are 1/4 inch thick plate glass and the top and bottom walls are wood. The tunnel velocity is controlled through a feedback loop and is capable of speeds up to 25 m/s. The wing is mounted from the wind tunnel test section ceiling using a 1/8 inch thick steel bar 1 inch wide with a rounded leading edge and faired trailing edge. By moving the ceiling panels, the wing can be located along the length of the test section, or approximately 1.8 m ahead of the five-hole probe measurement plane. The five-hole probe is a conical type Pitot probe 3.8 mm in diameter and is mounted on a computer controlled traversing sting. The sting can be traversed in the y-z plane (perpendicular to free-stream flow) by command from a PC and traversed in the x plane (parallel to free-stream flow) by hand. The probe is mounted on the sting parallel to the free-stream to minimize effects of probe interference from probe pitch or yaw. The probe extends approximately 100 mm ahead of the sting to minimize influence of the sting in the vortex. The 5 pressure ports are connected to a barocel manometer via a computer actuated valve relay bank, enabling any two ports to be measured differentially simultaneously. Between valve switches, a two second delay is allowed before measurement due to pneumatic lag. The wind tunnel setup is shown in figure 4.

The wake is first mapped using a low resolution large window pass. Once the locations of the vortices are determined, the region around a single vortex can be mapped at a maximum grid resolution of 1.9 mm, 1/2 the size of the probe or the distance between port orifices. Typical step sizes of 3.8 mm are used for most runs. Since four pressure measurements are taken at each point (one for upstream measurement, three for the 5-hole probe), each point takes approximately 10 seconds including sting movement. For a typical wake measurement, measurements are made in a 100 mm by 200 mm rectangular grid, resulting in a 27×54 grid or 1458 data points. Each run then takes approximately 4 hours to complete.

2.3 Towing Tank Setup

The tow tank experiments are conducted in the University of California-Berkeley Naval Architecture Offshore Engineering (UCB-NAOE) towing tank. The tank is approximately 70 m long and 2.4 m across with a nominal water depth of 1.5 m. A towing carriage moves along rails above the tank with a speed variable from $U = 10$ cm/s to 160 cm/s with an accuracy better than 1%. The tank has a viewing station near the center of the length of the tank consisting of a 3 m long window that extends from the tank bottom to the carriage rails. A light sheet is created in the tank using a 10 W Argon-ion laser. The sheet is approximately 5 mm thick and is placed perpendicular (cross-stream)

to the wing velocity as shown in figure 5. The regions immediately surrounding and upstream of the sheet are locally seeded with 40 μm silver-coated hollow glass spheres. The resulting light is imaged using a Sony XC-7500 30/60 Hz monochrome non-interlaced CCD camera with a 640×480 square-pixel sensing elements. A submersible stainless-steel vessel is used to house the camera. The vessel allows the camera lens to be focused and zoomed while underwater. This gives a near perpendicular viewing angle as opposed to our previous research while keeping the versatility of an unhoused camera [16, 17]. The vessel is shown in figure 6. The resulting images are captured and stored digitally in real-time on a PC using a Matrox Pulsar imaging board. Three hundred images at 30Hz are recorded in a typical run.

2.4 Data Processing

2.4.1 5-hole Pitot Probe

The 5-hole Pitot probe measures the differential pressure between any two ports. The probe is calibrated from $\pm 40^\circ$ pitch and yaw angle in 2° increments. To determine the freestream velocity deficit/surplus, the axial port and static port pressure difference is used. This is converted to velocity directly on a point-to-point basis. The horizontal and vertical ports are used to determine the y and z velocities, respectively. The smallest change in the flow angle $\Delta\Psi$ (yaw or pitch) that can be detected by the probe is determined by

$$\Delta\Psi = \frac{\Delta p_{min}}{(C_p)_\Psi \cdot (1/2)\rho U_\infty^2} \quad (1)$$

where Δp_{min} is the minimum pressure difference that can be measured and $(C_p)_\Psi$ is the yawmeter sensitivity.

In the 5-hole Pitot probe data, vorticity is determined from the measured y-z velocity field. To reduce smoothing since the data is a time-averaged sample, a 4-point finite difference method is employed. The intrusive effect of the probe on the vortex wake has been taken into consideration and is discussed in §3.1.1.

2.4.2 Lagrangian Parcel Tracking

The Lagrangian parcel tracking (LPT) algorithm developed by Sholl and Savaş [8] is used to determine instantaneous flow fields from the tow tank experiments. The LPT algorithm treats seeding particles as fluid parcel markers and tracks both their translations and deformations. During this tracking, fluid parcels registered by individual CCD pixels are advected with individually estimated velocities and total accelerations. The velocity field needed to initialize the LPT process is obtained from a standard DPIV algorithm which uses multiple passes, integer window shifting, and adjustable windows [7]. Both the LPT and DPIV algorithms employ a rigorous peak-detection

scheme to determine velocity vectors and use the local velocity gradient tensor to identify spurious velocity vectors. We have found that the LPT algorithm works well in the flow field of a vortex which is characterized by high deformation rates where DPIV algorithms are plagued by biasing and limited dynamic range. No smoothing algorithms or other post-processing techniques are employed on the data. In the tow tank data, vorticity, being a component of the velocity gradient tensor, is calculated spectrally at each grid point as an intrinsic part of the LPT algorithm.

3 Data Analysis

3.1 Wind Tunnel

3.1.1 Probe Effect

Quantifying the effect of the probe on the flow field is important and deserves some attention. It has long been suspected that intrusive probes may alter the motion and/or structure of a vortex. The evidence for this is mixed, however. Green & Acosta have found the presence of a probe can alter the location of the vortex core and may even lead to premature vortex breakdown [18]. The alignment of the probe was also found to be critical, indicating that a small pitch or yaw would have an effect on the flow characteristics where an aligned probe would not. Other studies tend to dismiss the effect of probe intrusion, however, citing observations and measurements that indicate the probe has a negligible effect on the structure of a vortex, including velocity profiles and turbulence levels, and does not induce vortex breakdown [19, 20, 21]. The majority of these intrusive measurements were made with hot-wires, however, which are typically much smaller than of a pitot probe. The question is then: at what size relative to the vortex does a probe begin to alter the flow? Two issues must be addressed: (1) the size of the probe in relation to the length scale of the flow structure may not properly resolve the flow, and (2) the size of the probe may change the flow field.

In the present case, the distance between the opposite end ports l_m is 1/2 the probe diameter, or 1.9 mm. The vortex core size, meanwhile, can generally be considered to be

$$r_c = b/10 \quad (2)$$

or

$$r_c = Re/10 \quad (3)$$

for an elliptically loaded rectangular wing assuming roll-up is complete [22]. Other estimates of core-size as a function of downstream distance are available, including a laminar 2-D vortex [23] and a vortex with axial flow [24], such that

$$r_c \approx 2\sqrt{\nu x/U_\infty} \quad (4)$$

where x is the downstream location and U_∞ is the free-stream velocity. For the simple assumption of equation 3, $r_c \approx 3.0$ cm. In this case, the size of the probe is relatively small ($l_m/r_c = 0.063$). Using equation 4, however, we see that $r_c \approx 10$ mm at $x/c = 4$, $r_c \approx 20$ mm at $x/c = 19$, and $r_c \approx 27$ mm at $x/c = 35$ giving a probe radius to vortex radius ratio of 0.19, 0.095, and 0.070, respectively. This is a significant fraction and may be large enough to appreciably alter the vortex characteristics. (A related question is the distance in which a vortex completely rolls up. The distance to complete roll-up for a tip vortex from an elliptically loaded wing is given by

$$x/c \sim AR^2/\lambda\pi\alpha \quad (5)$$

where α is the attack angle and λ is a scaling parameter ranging between 2 and 25 [25, 22, 26]. For the case presented here, $6 < x/c < 82$, a very wide range of downstream distances. Also note that for equation 4 to reach the value of r_c given by equation 3, $x/c = 4500$!) The size of the five-hole probe head and the distance between the pressure ports results in a relatively large measuring volume. (In the present case, the distance between the opposite end ports is 1/2 the probe diameter, or 1.9 mm. Due to the size and shape of a five-hole probe, the effect of the probe on the flow field can be accounted for in many situations [27].

3.1.2 Wake Decomposition

The resulting four pressures that are recorded from the five-hole probe are used to determine the three-dimensional velocity vector (with components $[u, v, w]$) from the axial velocity deficit and the yaw and pitch angles. Sample plots are shown in figures 8 and 9. The streamwise vorticity field is then calculated in the measurement plane by

$$\omega_x = \frac{\partial w}{\partial y} - \frac{\partial v}{\partial z} \quad (6)$$

using a finite difference algorithm. Circulation is obtained by a path integral of velocity

$$\Gamma = \int \mathbf{u} \cdot d\mathbf{l} \quad (7)$$

and is checked by summing the vorticity within the path, such as

$$\Gamma = \int \omega_x dA \quad (8)$$

In general, the first method is more accurate, as the vorticity within the center of the vortex core (or the peak vorticity) is not always well resolved. Due to this, the second method may give circulation values 10% lower than the first method, though for a well evolved vortex, the difference is typically 1%. Additional information such as lift and drag may be obtained from the wake survey using techniques outlined in Brune [28] and Takahashi [29].

3.2 Tow Tank

3.2.1 Effects of Stratification

Stratification plays an important role in wake vortex development; e.g., see Sarpkaya [30] or Spalart [14]. In the case of most experiments, such as in a typical towing tank or wind tunnel, media stratification does not play a significant role due to the small size of the test facility. The towing tank used for the experiments herein is large enough to warrant investigation of possible stratification effects, however.

The parameter governing stratification effects is

$$N^* = 2\pi N b^2 / \Gamma_o \quad (9)$$

where N , the Brunt-Väisälä frequency, is given by

$$N^2 = g\alpha \frac{dT}{dz} \quad (10)$$

with temperature, T , and coefficient of thermal expansion, $\alpha = (1/\rho)(\partial\rho/\partial T)$. Stratification is considered to start playing a role when $N^* \geq 0.1$ (though the role is initially small). Typical values for the stratification number for a full-sized aircraft in landing configuration are estimated to be

$$N^* \approx 0.6 \quad (11)$$

showing that stratification is indeed important while typical values for the tow tank are calculated to be

$$N^* \leq 0.01 \quad (12)$$

Thus, stratification can be considered to be negligible within the tank.

3.2.2 Flow Visualization

Flow visualization experiments were conducted using fluorescein dye. The dye was mixed with corn syrup and coated on the upper surface of the wings in chordwise strips. Once mounted on the carriage and immersed in the water, the dye would be released by the dynamic pressure over the moving wing in enough quantity to be visible by either the naked eye or in the laser sheet when fluorescing. The flow visualization were used as a guide to global behavior prior to PIV measurements. They were also useful in visualizing instabilities on a vortex surface. A sample flow visualization run is shown in figure 7.

3.2.3 LPT Results

Since LPT results in a series of instantaneous snapshots of the 2-D velocity and vorticity fields, the data allows a number of possibilities. The tangential velocity and vorticity profiles can be analyzed as the vortex evolves downstream. Quantities such as vortex core radius, peak vorticity, circulation, impulse, etc., can also be examined in this manner. Using Taylor's frozen field hypothesis, one can also construct three-dimensional isovorticity contour of the flow field. As long as the wake remains in the field of view, data can be obtained. Typical measurement times range from 10 to 30 s. Since the airfoil is moving on the order of 100 cm/s, this translates into measurement distances of approximately 200 to 600 chord lengths downstream. This allows controlled detailed measurement of vortex evolution within the wake at downstream locations that has been previously unavailable.

4 Results

4.1 The Strut Wake

Preliminary tests in the tow tank were performed using an aerodynamically faired strut, as mentioned previously. Visual observations and velocimetry results showed poor formation of the flap vortex resulting in a rapid merger or mutual destruction of the flap vortices. This was attributed to the turbulent wake of the strut disrupting the roll-up of the vortex sheet. Subsequent tests in the tow tank using the thinner strut showed no such problems with the roll-up of the flap vortices. This was quantified in the wind tunnel by performing identical airfoil tests with the different struts.

The effect of the strut wake is illustrated in figures 8 and 9, which show two three-dimensional velocity plots from the wind-tunnel tests of the 30% flap arc airfoil taken at $x/c = 5$ downstream of the wing. In figure 8, the thick streamlined strut is used. In figure 9, the thin flat plate strut is used. In each plot, the wake from the strut is seen at the left. The thick streamlined strut's wake is clearly much larger than that of the thinner strut, effectively reducing the downwash at the centerline and disrupting the vortex sheet. The maximum azimuthal velocity of the flapped vortex is also smaller.

Further evidence of the strut is shown in figures 10 and 11. In each, comparisons of vortex strength are made at three downstream stations, $x/c = 5$, $x/c = 20$, and $x/c = 35$. Figure 10 shows results for the 30% flap wing. At the first downstream station, the strengths of the flap and tip vortices for each case are approximately equal. As the wake evolves downstream, the strength of the tip vortices for each case gradually increases as the roll-up process is completed (the dip at $x/c = 20$ is due to the tip vortex being partially out of the measurement window). This is not the case for the flap vortex, however. For the flat-plate strut, note that the vortex strength is approximately constant from station to station, indicating that the roll-up occurs very quickly

for the flap vortex, which should be the case for a flap relatively close to the centerline. For the streamlined strut, the vortex strength strength is approximately the same at $x/c = 5$ but decreases monotonically from $x/c = 20$ to $x/c = 35$. The strut has disrupted the vortex sheet causing a premature breakdown of the vortex. At $x/c = 35$, the flap vortex is three times as strong in the flat-plate case compared to the streamlined strut case, while the tip vortices are of equal magnitude. Similar results for the 67% flap wing are shown in figure 11, but the decrease in the strength of the flap vortex is not as severe. This is due to the larger flap-span ratio of the wing, limiting the effect of centerline disruption on the development of the vortex. The decrease in strength of the flap vortex at $x/c = 35$ is approximately 30% from case to case.

A cartoon of the effect of the strut on the wake is shown in figure 14. Here it is shown how the wake is disrupted by turbulence. Since the flap vortices are formed almost exclusively from the vorticity within the sheet between the airfoil centerline and the flap location, a disruption will result in a decrease in the strength of the flap vortex. Using the same strut on airfoils with different flap-spans will result in different percentages of reduction in the circulation; viz. the 30% flap-span wing will have a much larger reduction in vortex strength than the 67% flap-span wing. Since the strut wake is limited to the immediate region behind it, the tip vortex should remain unaltered.

4.2 Angle of Attack and Wing Stall

Figures 12 and 13 show the effect of the angle of attack on initial vortex strength for the 30% and 67% flap wings, respectively. Three angles of attack α are plotted, 4° , 8° , and 12° . The tip vortex strength for both wings increases not only monotonically, but linearly as predicted by classical wing theory. This is not the case for the flap vortices, however. In both the 30% and 67% flap wings, the flap vortex strength increases approximately 25% at $\alpha = 8^\circ$ from $\alpha = 4^\circ$. At $\alpha = 12^\circ$, however, the strength of the flap vortex returns to its near $\alpha = 4^\circ$ value. Examining the vortex plots (see appendix) show stream-wise vortices forming between the flap and tip vortices at $\alpha = 8^\circ$, possibly due to stall. These vortices disappear at $\alpha = 12^\circ$.

4.3 Vortex Merger

Figure 15 shows two vortex merger sequences from tow tank experiments. Figure 15a is for the 67%-flap wing and figure 15b for the 30%-flap wing. Both wings are at a 4° angle of attack and being towed at 160 cm/s. The flows are recorded at different magnifications and processed at the same CCD window size. Hence, the processing window sizes are different: $0.042b \times 0.042b$ for the 67%-flap wing and $0.064b \times 0.064b$ for the 30%-flap wing. One half of each wing is shown. Contour base values and increments are the same in all frames. The *zero* contour is not shown in order to mask the background noise. The vortex shapes are distorted at the planes of wings $z = 0$, which

nearly coincide with the edges of the data fields. The frame times are indicated at the lower left corners and tip vortices are labeled as T. The frames are presented at about $\pi/4$ radian rotation increments of the pairs except the last frame which is about $\pi/2$ radians after the preceding frame.

Both sequences show that the vortices coming off the wings orbit around each other in the counter-clockwise direction under the influence of their respective induced velocities and descend under the influence of the vortex system coming off the other half of the wing. This behavior is typical when the Reynolds number is sufficiently high, which can be achieved by increasing either the towing speed, the angle of attack or both. At low Reynolds numbers, the vortices diffuse before they interact and will not be discussed further. The vortex merger in the wake of the 67%-flap wing occurs quickly by $z/b \sim 0.20$. The distributed vortex wake is clearly visible $t = 0$ where the tip and the flap vortices have formed. The true strength of the tip vortex becomes visible when it has moved down. The flap vortex is visibly distorted and is wrapped around the tip vortex, which dominates the flow field. The final single vortex keeps descending along $y/b \sim 0.33$. The merger in the wake of the 30%-flap wing takes much longer than that of the 67%-flap wing. The tip vortex dominates the flow field. The first signs of merger appear around $z/b \sim 0.4$ where the flap vortex is being strained and is changing its shape. By the time the pair reaches about $z/b = 1$, the flap vortex is torn apart and is being incorporated into a single vortex which continues its descent along $y/d \sim 0.37$. We observe in both sequences in figure 15 that the vortex merger takes about one orbit time of the pair. The descent distance to merger, however, depends on the wing characteristics.

Preliminary results are shown in the figures displaying the effect of the non-airfoil wake on the vortex wake formation. In figure 16, results from multiple tow tank runs show the descent distance for the same-signed tip and flap vortices to merge. Two trends are worth noting. First, from these measurements, it appears that the merger distance is monotonic with flap-span. That is, as the extend of the flap gets larger, the vertical descent to merger get smaller. Second, the type of strut used to connect the airfoil to the towing carriage has a large effect on the merger distance. For the 30% span flap arc airfoil, the merger distance is doubled by using a thin flat plate strut rather than a thick streamlined strut. The wake of the strut interferes with the roll-up of the vortex sheet into a coherent vortex, as shown in figure 14. The tip and the flap vortices form from roll-up of the vortex sheet. The strut wake disrupts the vortex sheet between the flap-tips, inhibiting the formation of the flap vortices. This leads to weaker flap vortices, which merge more quickly with the tip vortices.

The merging process of two like-signed vortices is not yet fully understood, though there has been much research into the phenomenon. The end result of the physics has been to try to quantify relations for a critical parameter, which can predict when two vortices will merge, based upon their physical characteristics such as separation distance, comparative strength, shape, age, etc.

Our measurements suggest that as the vortices orbit one another, they are distorted due to the velocity gradients and pulled into each other. Three-dimensional simulations tend to show similar results though merger is highly dependent upon the initial vortex separation [31]. The effect of the three-dimensionality of the vortices cannot be understated.

Figure 16 shows the time to merger for a number of vortices. Observations clearly show that the vortices always merge after approximately one orbit of one another. If the descent velocity (downwash) is taken to be

$$U_d = \frac{\Gamma_s}{2\pi\beta} \quad (13)$$

where Γ_s is the sum of the flap and tip vortices' circulation and β is the separation distance of the two pairs, then after one orbit, the vortices have descended a distance

$$h = U_d \cdot t = \left(\frac{\Gamma_s}{2\pi\beta}\right) \left(\frac{4\pi^2 i^2}{\Gamma_s}\right) = 2\pi i^2 \beta \quad (14)$$

where i is the initial separation between the flap and tip vortices. Then,

$$h/b = 2\pi(i/b)^2(b/\beta) \quad (15)$$

where i/b is the tip-flap vortex separation to tip-tip vortex separation ratio and b/β is the initial to final tip-tip vortex separation ratio [32]. This result indicates that merger is a function of wing geometry (planform) alone. If we assume that $\beta \approx \frac{\pi}{4}b$, then

$$h/b \approx 8(i/b)^2 \quad (16)$$

Since i and b are related by the wing geometry namely the span flap ratio $\kappa = b_f/b$, we can write

$$i = \frac{1}{2}(b - \kappa b) \quad (17)$$

so that

$$h/b \propto 2(1 - \kappa)^2 \quad (18)$$

Note that the vortex mergers of wakes with the thick strut fall far off of the line while cases of the flapped wings using the thin strut fall on or close to the line given by equation 18. It can be argued that the latter cases are more “ideal,” i.e., the flat plate strut disrupts the natural wake of the wing less than that of the thicker streamlined strut. The effect may be analagous to that of a fuselage on the wing wake: aerodynamically dirty fuselages may effect the wake so that the flap and tip vortices merge more quickly than an identical wing wake of an aircraft with a cleaner structure.

For a detailed summary of experiments conducted on vortex merger, see [33].

5 Summary

The dynamics of trailing vortex wakes from flapped airfoils are investigated in a towing tank and a wind tunnel. The wakes from a lifting rectangular circular arc airfoil with an aspect ratio of 6 and flap-spans of 30% and 67% are studied up to 300 chords downstream in the tow tank and up to 35 chords in the wind tunnel. Chord Reynolds numbers ranged from $1.5 \cdot 10^4$ to $8 \cdot 10^4$. A traversing five-hole Pitot probe and a novel Lagrangian parcel tracking (LPT) algorithm are used to measure the velocity field in a cross-stream plane behind the wings in the wind tunnel and the towing tank, respectively. The interaction of the tip and the flap vortices are observed. The strut wake is shown to have a significant effect on the wake vortex development, reducing the strength of the flap vortices for struts with “thick” turbulent wakes. At low Reynolds numbers, the vortices decay before they have significant interaction. At high Reynolds numbers, the vortices merge before diffusion significantly alters them. The merger of the flap and the tip vortices usually occurs within one orbit, leading to a shorter descent distance to merger for longer flap-spans.

References

- [1] B. D. Nordwall. Wake turbulence tests to determine safe separation. *Aviation Week & Space Technology*, page 85, Nov. 21 1994.
- [2] E. H. Phillips. Vortex tests may yield clues to USAir crash. *Aviation Week & Space Technology*, page 33, Oct. 2 1995.
- [3] AGARD. *78th Fluid Dynamics Panel Symposium on the Characterization and Modification of Wakes from Lifting Vehicles in Fluids*, 1996. NATO-AGARD-CP-584.
- [4] J. Vasatka. The dynamic response of a twin-engine, commercial jet transport to wake vortex encounters. In *78th Fluid Dynamics Panel Symposium on the Characterization and Modification of Wakes from Lifting Vehicles in Fluids*. AGARD, 1996. NATO-AGARD-CP-584-14.
- [5] J. D. Jacob, Ö. Savaş, and D. Liepmann. Aircraft wake turbulence and airport capacity. *Institute of Transportation Studies Review, University of California at Berkeley*, 19(4), August 1996.
- [6] Y.-C. Cho. Digital image velocimetry. *Applied Optics*, 28:740–748, 1989.
- [7] C. E. Willert and M. Gharib. Digital particle image velocimetry. *Experiments in Fluids*, 10:181–193, 1991.

- [8] M. J. Sholl and Ö Savaş. A fast Lagrangian PIV method for study of general high-gradient flows. In *AIAA 35th Aerospace Meetings & Exhibits*. AIAA, 1997. Paper 97-0493.
- [9] J. D. Jacob. *Experimental investigation of the trailing vortex wakes of rectangular airfoils*. PhD thesis, University of California at Berkeley, 1995.
- [10] J. D. Jacob, Ö Savaş, and D. Liepmann. Experimental investigation of forced wake vortices of a rectangular wing. In *AIAA 14th Applied Aerodynamics Conference Proceedings*. AIAA, 1996. Paper 96-2497.
- [11] J. D. Jacob, Ö. Savaş, and D. Liepmann. Trailing vortex wake growth characteristics of a high aspect ratio rectangular airfoil. *AIAA Journal*, 35(2):275–280, February 1997.
- [12] A. J. Bilanin, M. E. Teske, and G. G. Williamson. Vortex interactions and decay in aircraft wakes. *AIAA Journal*, 15(2):250–260, 1977.
- [13] D. G. Dritschel. A general theory for two-dimensional vortex interactions. *Journal of Fluid Mechanics*, 293:269–303, 1995.
- [14] P. R. Spalart. On the motion of laminar wing wakes in a stratified fluid. *Journal of Fluid Mechanics*, 327:139–160, 1996.
- [15] J. D. Crouch. Stability of multiple trailing-vortex pairs. In *78th Fluid Dynamics Panel Symposium on the Characterization and Modification of Wakes from Lifting Vehicles in Fluids*. AGARD, 1996. NATO-AGARD-CP-584-17.
- [16] Ö. Savaş, J. L. Rodriguez Azara, and D. Liepmann. On seeding and optical arrangements for DPIV. Technical Report UCB-FML Technical Report, Dept. of Mechanical Engineering, University of California, Berkeley, CA, 1995.
- [17] J. D. Jacob and Ö Savaş. Vortex dynamics in trailing wakes of flapped rectangular wings. In *AIAA 35th Aerospace Meetings & Exhibits*. AIAA, 1997. Paper 97-0048.
- [18] S. I. Green and A. J. Acosta. Unsteady flow in trailing vortices. *Journal of Fluid Mechanics*, 227:107–134, 1991.
- [19] D. L. Ciffone and K. L. Orloff. Far-field wake-vortex characteristic of wings. *Journal of Aircraft*, 12(5):464–470, 1975.
- [20] J. D. Iverson, V. R. Corisiglia, S. Park, D. R. Backhus, and R. A. Brickman. Hot-wire, laser-anemometer, and force measurements of interacting trailing vortices. *Journal of Aircraft*, 16:448–454, 1979.

- [21] W. J. Devenport, M. C. Rife, S. I. Liapis, and G. J. Follin. The structure and development of a wing-tip vortex. *Journal of Fluid Mechanics*, 312:67–106, April 1996.
- [22] J. R. Spreiter and A. H. Sacks. The rolling up of the trailing vortex sheet and its effect on downwash behind wing. *Journal of the Aeronautical Sciences*, 18:21–32, 1951.
- [23] B. G. Newman. Flow in a viscous trailing vortex. *Aeronautical Quarterly*, pages 140–160, May 1959.
- [24] G. K. Batchelor. Axial flow in trailing line vortices. *Journal of Fluid Mechanics*, 20:645–658, 1964.
- [25] P. G. Saffman. *Vortex Dynamics*. Cambridge University Press, New York, NY, 1992.
- [26] S. C. Crow. Stability theory for a pair of trailing vortices. *AIAA Journal*, 8:2172–2179, 1970.
- [27] F. Vinnemeier, L. Simon, and W. Koschel. Korrektur des Kopfgeometrieinflusses einer Fünfloch-Drucksonde auf die Meßergebnisse. *Technisches Messen tm*, 57:266–303, 1990.
- [28] G. W. Brune. Quantitative low-speed wake surveys. *Journal of Aircraft*, 31(2):249–255, 1994.
- [29] T. T. Takahashi. On the decomposition of drag from wake survey measurements. In *AIAA 35th Aerospace Meetings & Exhibits*. AIAA, 1997. Paper 97-0717.
- [30] T. Sarpkaya. Trailing vortices in homogeneous and density stratified media. *Journal of Fluid Mechanics*, 136:85–100, 1983.
- [31] T. Matsushima. *Spectral Methods in Polar Coordinates with an Application to the Stability of a Trailing Vortex*. PhD thesis, University of California at Berkeley, 1995.
- [32] A. Chen, J. D. Jacob, and Ö. Savaş. Dynamics of corotating vortex pairs in the wakes of flapped airfoils. In preparation.
- [33] A. Chen, J. D. Jacob, and Ö. Savaş. ISOVORS, 1997. Institute of Transportation Studies, University of California at Berkeley.

A Tables & Figures

run	b_f/b	α [$^\circ$]	x/c	Γ_{tip} [cm ² /s]	Γ_{flap} [cm ² /s]	comments
960510	0.30	4	5	762	1176	thick strut
960513	0.30	4	5	756	1339	
960603a	0.67	4	5	1597	1522	thick strut
960603b	0.67	4	5	1518	1471	
960604a	0.67	4	20	2192	1745	
960604b	0.67	4	20	1944	1452	thick strut
960605a	0.30	4	20	496*	1356	
960605b	0.30	4	20	615	886	thick strut
960606a	0.30	4	35	1308	1533	
960606b	0.30	4	35	1324	457	thick strut
960607a	0.67	4	35	2108	1721	
960607b	0.67	4	35	1977	1247	thick strut
960608a	0.67	8	5	2918	1894	
960608b	0.67	12	5	4250	1724	
960609a	0.30	8	5	2056	1524	
960609b	0.30	12	5	3395	1421	
960721a	0.30	4	5	1706	1811	2 engines (no thrust)
960722a	0.67	4	5	2060	1628	2 engines (no thrust) [†]
960727a	0.67	4	5	1843	2141	4 engines (no thrust) [‡]

Table 1: Wind tunnel parameters.

*Poorly resolved.

[†]Additional vortex due to engine: $\Gamma = 243$ cm²/s.[‡]Additional vortex due to engine: $\Gamma = 358$ cm²/s.

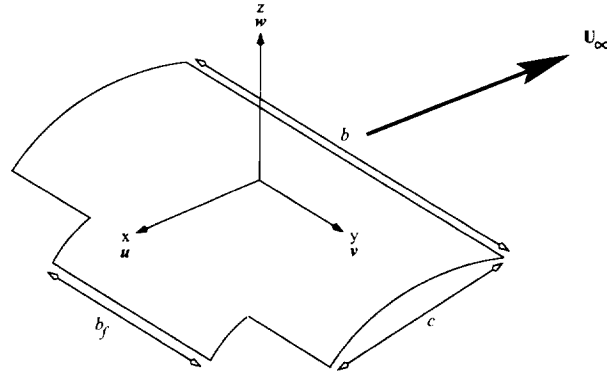


Figure 1: Coordinate system and airfoil designations.

The wing dimensions are $b = 305$ mm and $c = 51$ mm. Two flap-spans are available, $b_f/b = 0.30$ and $b_f/b = 0.67$.

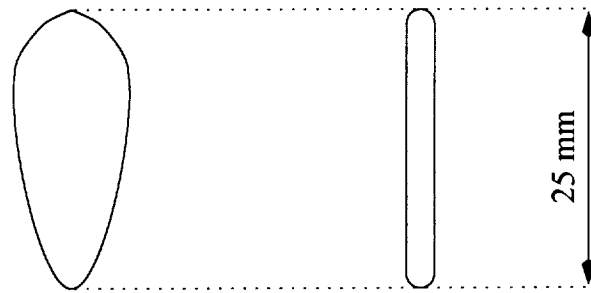


Figure 2: Relative strut sizes.

The streamlined strut (left) and the flat plate strut (right) both have a chord of approximately 25 mm.

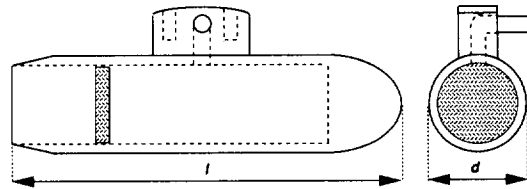


Figure 3: Wing engines.

The engines are constructed of stainless steel. $l = 40$ mm and $d = 15$ mm. The leading edge is a 2:1 parabolic profile.

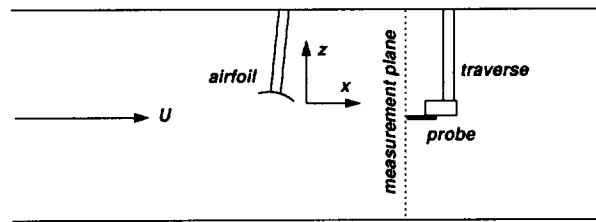


Figure 4: Wind tunnel.

The test section is 0.81 m square. $U \leq 25$ m/s.

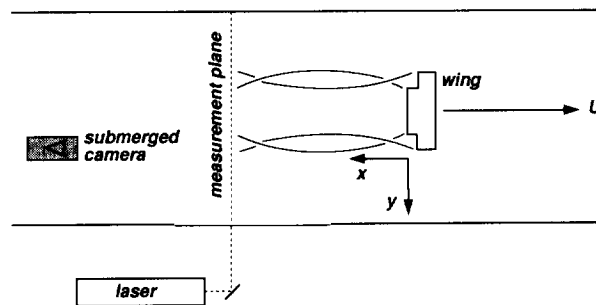


Figure 5: Towing tank.

The tank is 2.4 m wide, 1.7 m deep, and 70 m long. $U \leq 160$ cm/s.

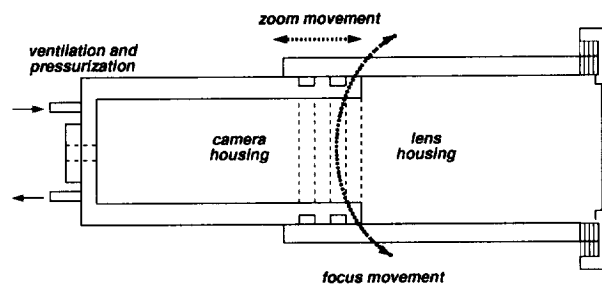


Figure 6: Submersible camera vessel.

The airtight vessel is used to house a CCD camera and lens.

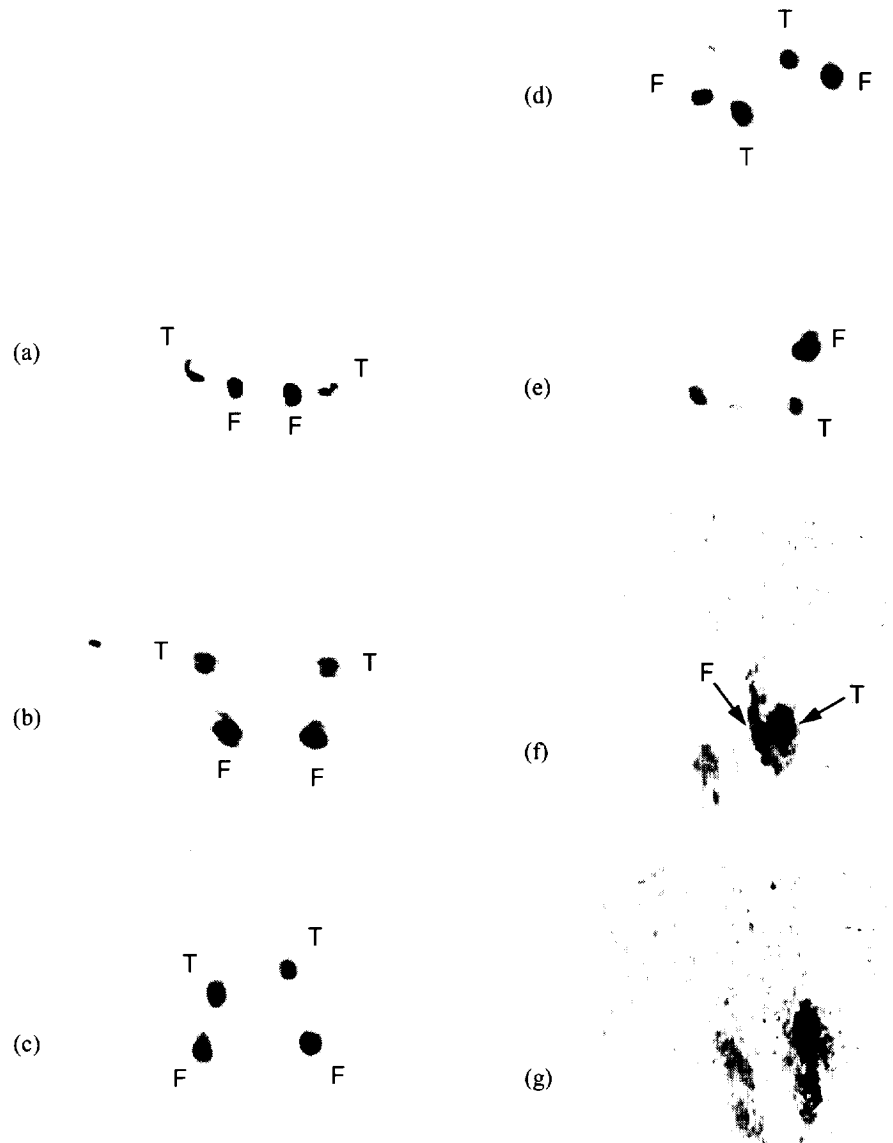


Figure 7: Flow visualization of flapped wing.

Enhanced photographs of flow visualization of the vortex wake of the 30% flap-span airfoil. The flap vortices are generally the darker colored vortex and are marked by a F while tip vortices are marked by a T. (a) is taken immediately after the wing passes through the laser sheet and subsequent images are at unequal intervals. By (f), after a single rotation, the right vortex pair has almost completed merger. The dye in the left vortex pair is no longer easily visible, possibly due to increased diffusion in the merger process.

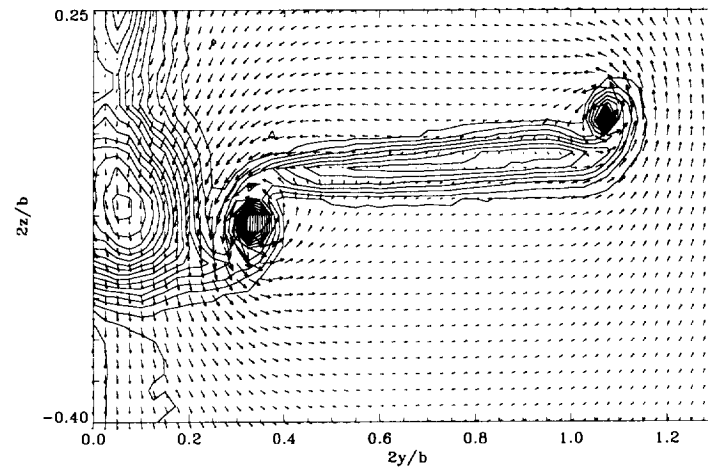


Figure 8: 30% flap with streamlined strut.

The contours show the velocity deficit, i.e. free-stream velocity field. The vectors show the in-plane velocity components.

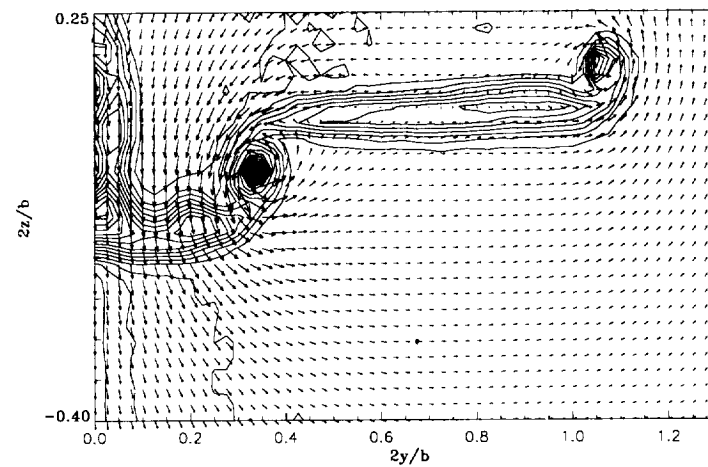


Figure 9: 30% flap with flat-plate strut.

The contours show the velocity deficit, i.e. free-stream velocity field. The vectors show the in-plane velocity components.

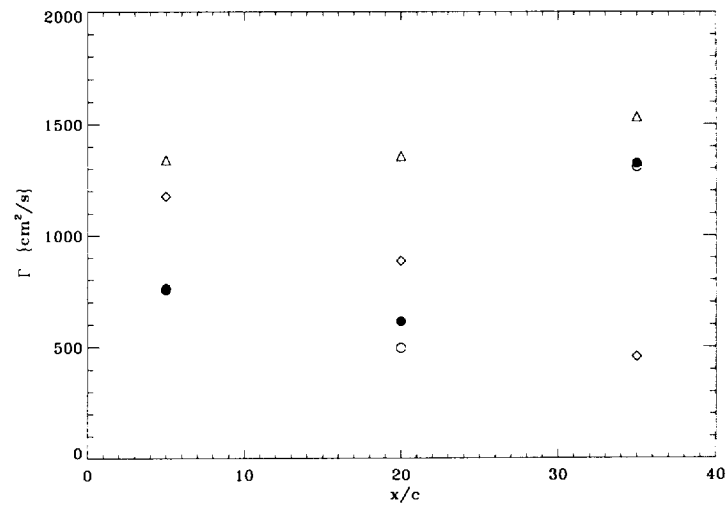


Figure 10: Effect of strut on vortex roll-up.

30% flap case: ○, tip vortex, thin strut; ●, tip vortex, thick strut; △, flap vortex, thin strut; ◇, flap vortex, thick strut.

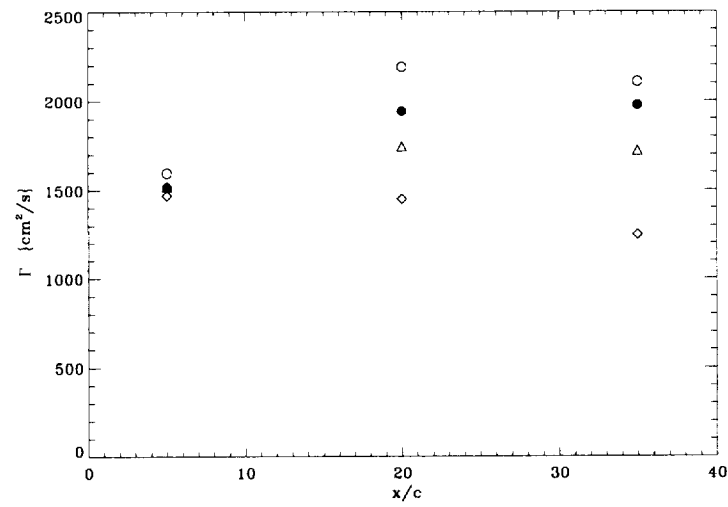


Figure 11: Effect of strut on vortex roll-up.

67% flap case: ○, tip vortex, thin strut; ●, tip vortex, thick strut; △, flap vortex, thin strut; ◇, flap vortex, thick strut.

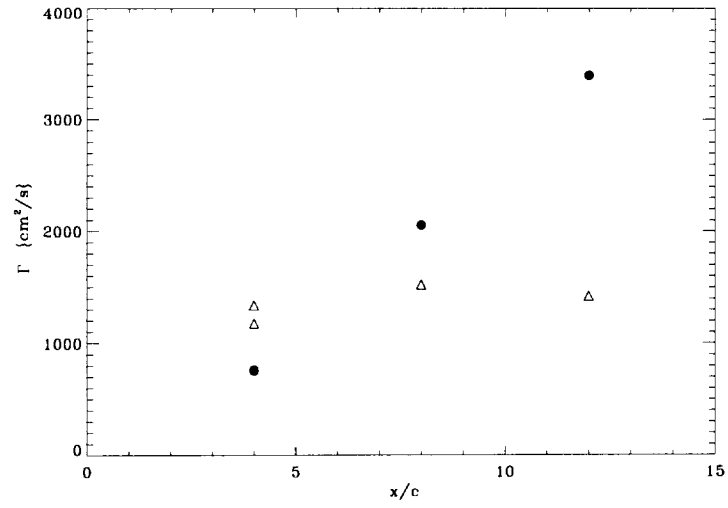


Figure 12: Effect of angle of attack on initial vortex strength.

30% flap case: ●, tip vortex; Δ, flap vortex.

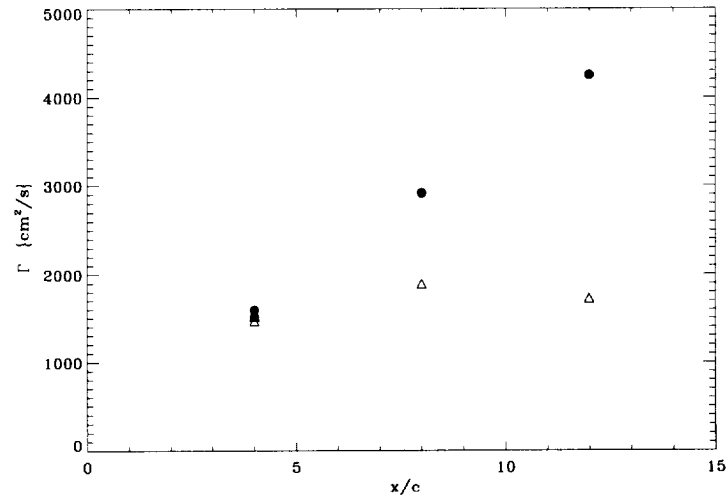


Figure 13: Effect of angle of attack on initial vortex strength.

67% flap case: ●, tip vortex; Δ, flap vortex.

Re_c and Re_Γ for wind tunnel and tow tank runs.

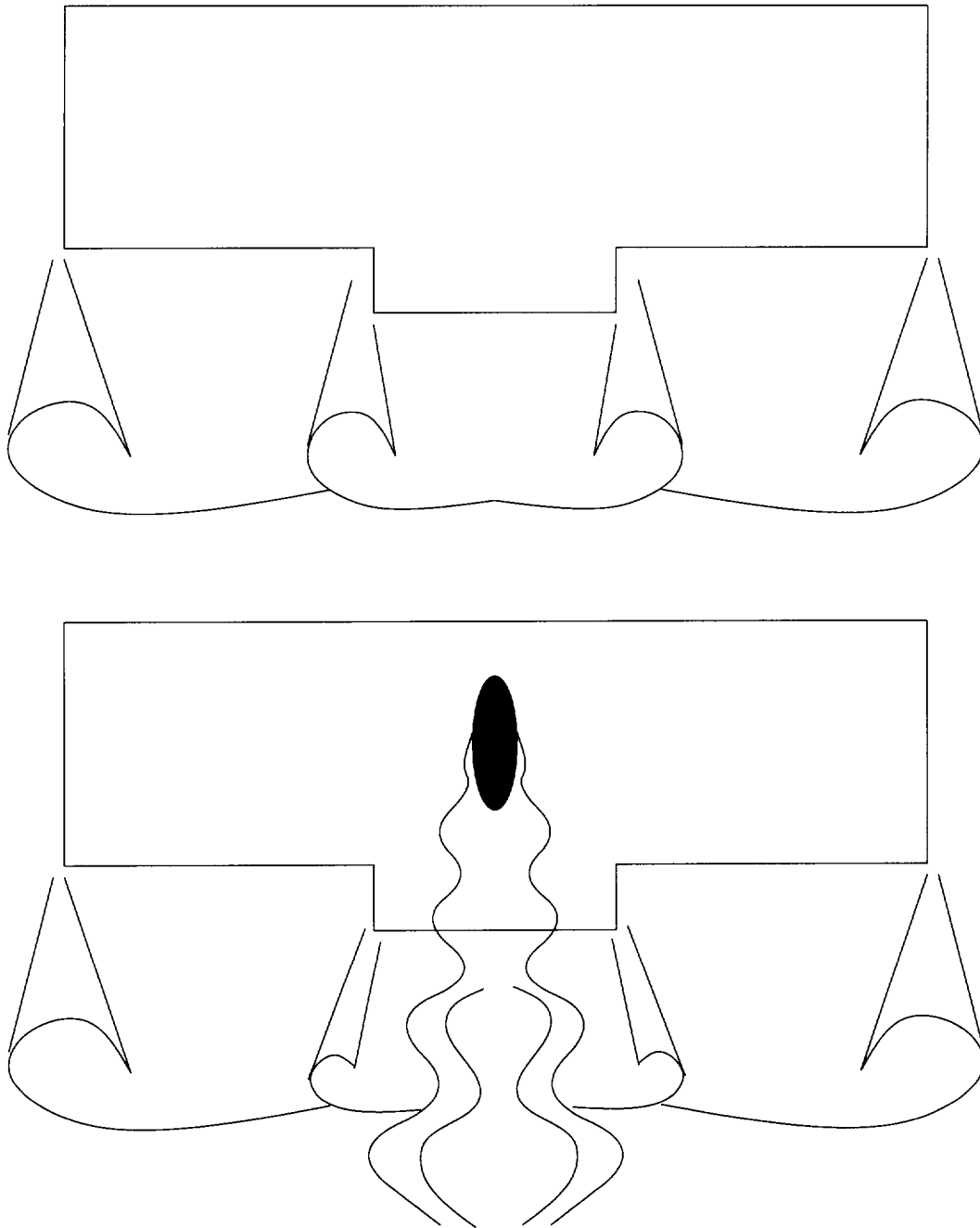


Figure 14: Cartoon showing disruption of the wake.

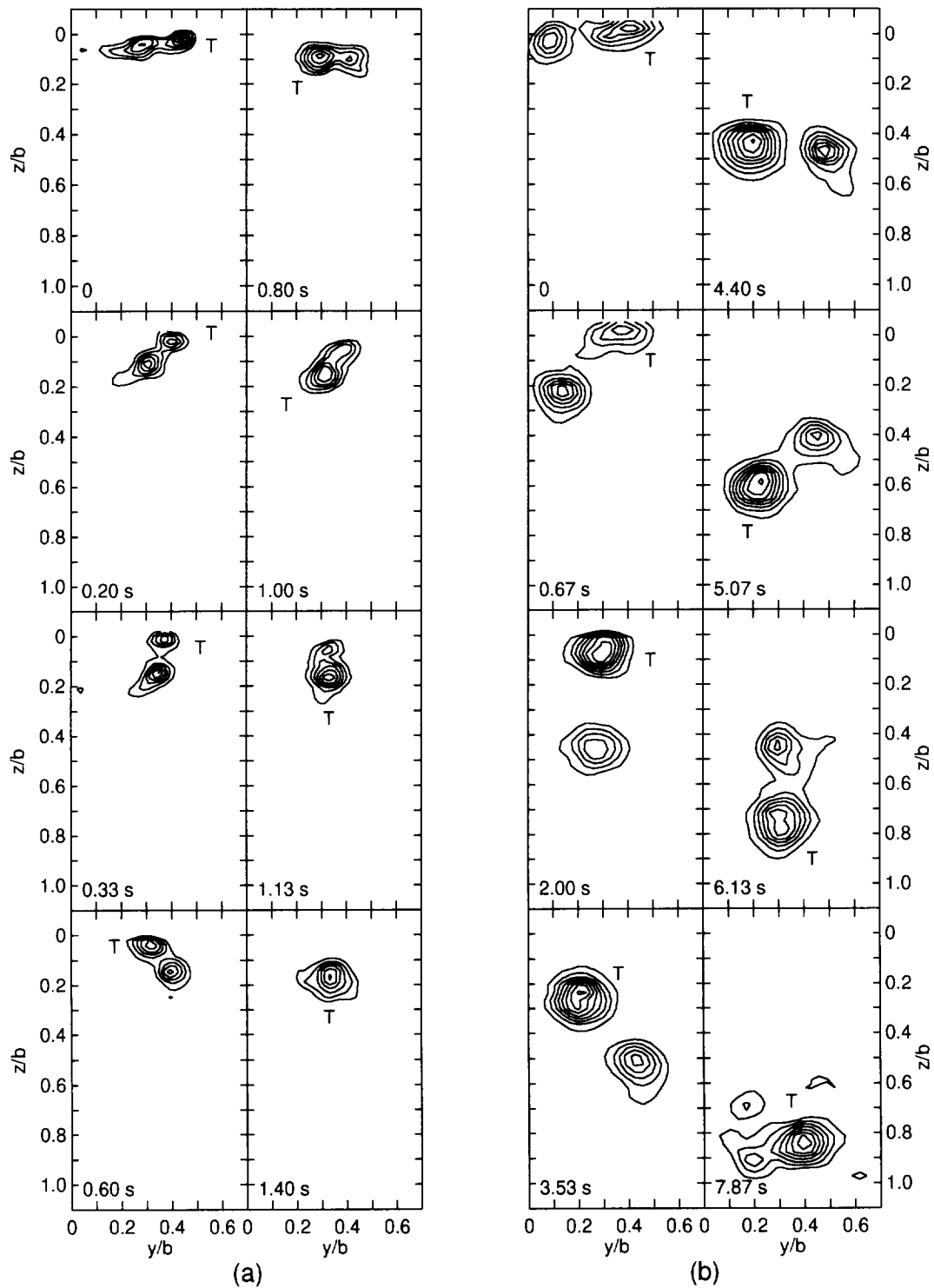


Figure 15:

Merger of same signed wake vortices off flapped circular airfoils. LPT measurements in towing tank. Contour base values and increments are the same for all frames. $U = 160$ cm/s, and $\alpha = 4^\circ$. Frame times are indicated in the lower left corners and the tip vortex is labeled as T. (a) 67%-flap airfoil and (b) 30%-flap airfoil.

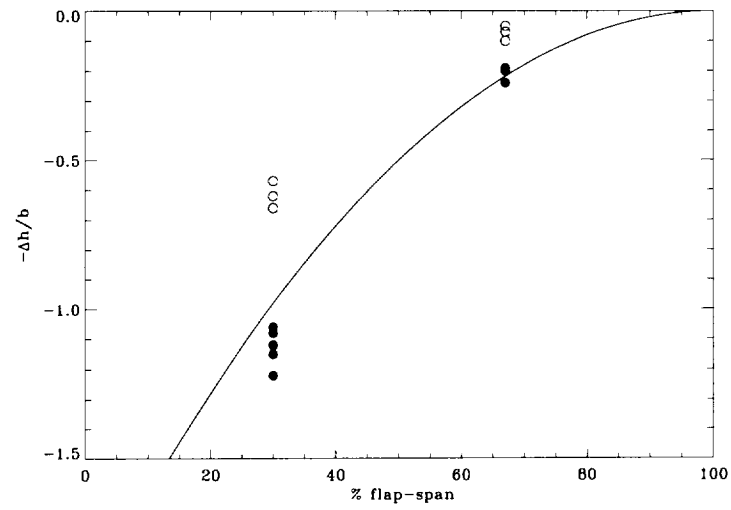


Figure 16: Vortex merger descent distances.

Descent distance for the flap and tip vortices to merge. Note that the merger distance for the 30%-flap case is doubled by changing struts. The solid line indicates the curve given by $h/b \propto 2(1 - \kappa)^2$.

B Wind Tunnel Vorticity Plots

The following vorticity plots are given as a catalog for the wind tunnel runs. Refer to table 1 for information on each run.

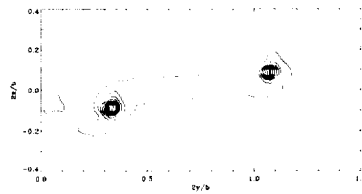


Figure 17: Wind tunnel run 960510.

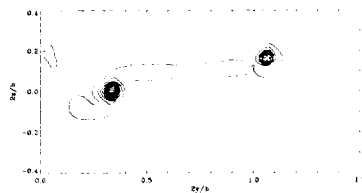


Figure 18: Wind tunnel run 960513.

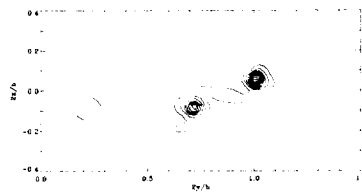


Figure 19: Wind tunnel run 960603a.

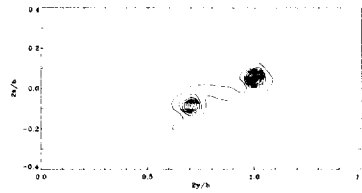


Figure 20: Wind tunnel run 960603b.

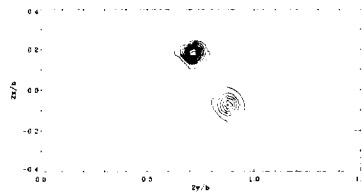


Figure 21: Wind tunnel run 960604a.

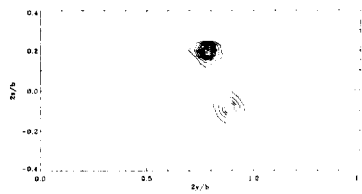


Figure 22: Wind tunnel run 960604b.

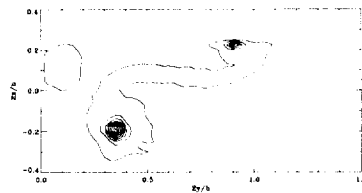


Figure 23: Wind tunnel run 960605a.

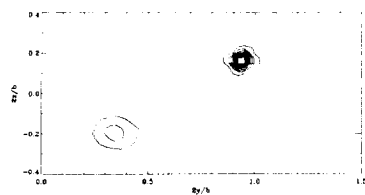


Figure 24: Wind tunnel run 960605b.

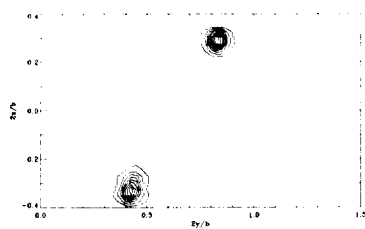


Figure 25: Wind tunnel run 960606a.

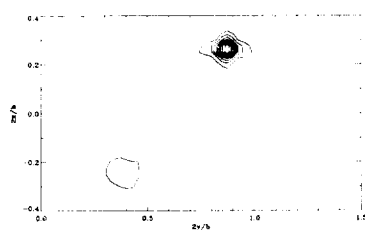


Figure 26: Wind tunnel run 960606b.

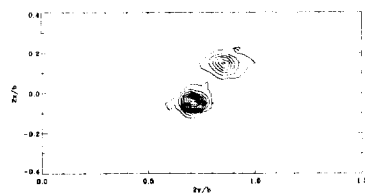


Figure 27: Wind tunnel run 960607a.

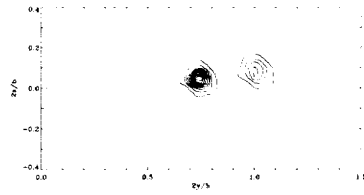


Figure 28: Wind tunnel run 960607b.

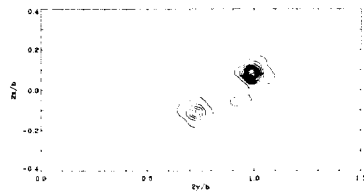


Figure 29: Wind tunnel run 960608a.

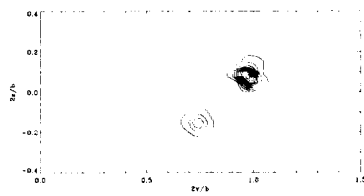


Figure 30: Wind tunnel run 960608b.

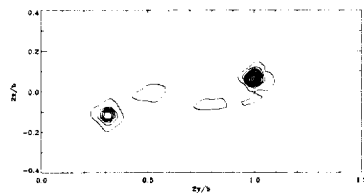


Figure 31: Wind tunnel run 960609a.

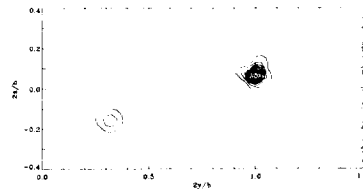


Figure 32: Wind tunnel run 960609b.

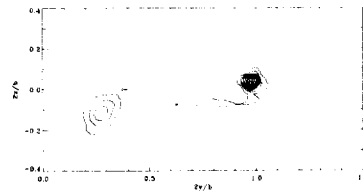


Figure 33: Wind tunnel run 960721a.

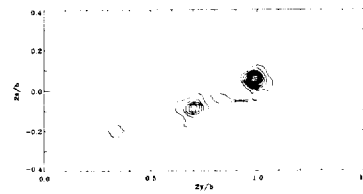


Figure 34: Wind tunnel run 960722a.

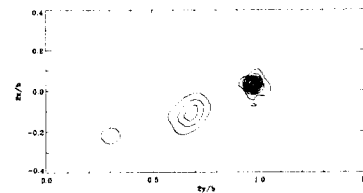


Figure 35: Wind tunnel run 960727a.